Supplementary Material: Real-Time Quantum Vacuum Control in a Photonic Integrated Circuit

Ying Wang[1, †, *], Celeste Qvotrup[1, †], Marcus Albrechtsen[1], Rodrigo Thomas[1], Zhe Liu[1], Sven Scholz[2], Arne Ludwig[2], and Leonardo Midolo[1]

[1]Center for Hybrid Quantum Networks (Hy-Q), Niels Bohr Institute, University of Copenhagen, Blegdamsvej 17, Copenhagen, 2100, Denmark
[2]Lehrstuhl für Angewandte Festkörperphysik, Ruhr-Universität Bochum, Universitätsstrasse 150, D-44780 Bochum, Germany

[†]These authors contributed equally to this work.
[*]Corresponding authors: yingwangnbi@gmail.com, midolo@nbi.ku.dk

Contents

A Control of Spontaneous Emission

To describe the dynamics of the interaction between QDs and the optical modes, a complete layout is shown in S1. The waveguide is oriented along the x-axis, with the mirror plane defined at $x = 0$. The physical and image systems therefore lie on the $x > 0$ and $x < 0$ sides of the mirror plane, respectively. The lateral center of the waveguide is defined by $y = 0$, while $z = 0$ denotes the center of the waveguide along its thickness, where the QDs are positioned. The coupling of the x- and y-polarized neutral-exciton transition dipoles to the waveguide mode is determined by the lateral offset y_0 from the waveguide center. The mirror is located at a distance $|x_{\mathrm{m}}| = L$ from the QD. A mirror displacement Δx introduces a tunable single-pass phase $\phi = k\Delta x$, resulting in a round-trip phase shift of 2ϕ. The complex amplitude reflection coefficient can therefore be written as $r_{\mathrm{T}} = |r_{\mathrm{T}}|e^{i2\phi}$. The electric field at the position of the emitter is given by

$$\mathbf{E}(0, y_0, z_0) = \bar{\mathbf{E}}(y_0, z_0) + |r|\bar{\mathbf{E}}^*(y_0, z_0)e^{-i2(kL+\phi)} \tag{S1}$$

where the first term is the transmission field of the QD-WG sytem while the second term represents the field reflected by the mirror and returning to the emitter. We denote with $\bar{\mathbf{E}}(\mathbf{y},\mathbf{z})$ the transverse eigenfunctions of the waveguide, which can be obtained solving Helmoltz' equation numerically for the specific waveguide shape. In rectangular waveguides the transverse-electric modes at $z = 0$, i.e. where the QDs are located, a good approximation for the transverse eigenfunction is $\bar{\mathbf{E}} = (ie_x(y), e_y(y), 0)$, with e_x and e_y purely real functions. The light intensity radiated by the an $x-$dipole at the origin is thus:

$$I_x = \frac{cn\varepsilon_0}{2}|e_x(y_0)|^2\left[1 + |r_{\mathrm{T}}|^2 + 2|r_{\mathrm{T}}|\cos(2\phi + 2kL)\right], \tag{S2}$$

whereas for a $y-$dipole:

$$I_y = \frac{cn\varepsilon_0}{2}|e_y(y_0)|^2\left[1 + |r_{\mathrm{T}}|^2 - 2|r_{\mathrm{T}}|\cos(2\phi + 2kL)\right]. \tag{S3}$$

Thus, as expected, the radiated power oscillates sinusoidally with the relative distance from the mirror L and the variable phase ϕ. The visibility of the intensity collected at the grating is independent of the lateral offset y_0 for a given dipole orientation. However, if both dipoles are excited equally (we assume this is the case under above-band excitation) the visibility is modified as shown in Eq. S11, which could explain the fact that different emitters show different interference visibilities and could provide a way to estimate the lateral offset of the emitter.

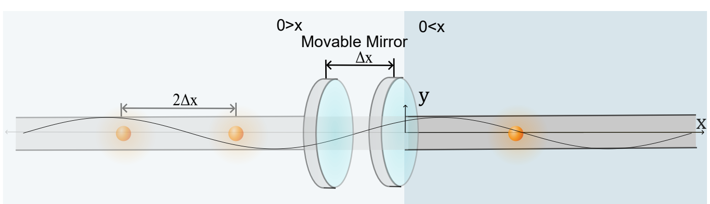

Figure S1: Extension of a QD-WG system integrated with a movable mirror to include its image representation. The mirror plane is located at $x = 0$, separating the physical system at $x > 0$ from the image system at $x < 0$. The phase of the QD image dipole is determined by the mirror position. A mirror displacement of Δx changes the separation between the real and image dipoles by $2\Delta x$, corresponding to the round-trip optical phase shift.

The spontaneous emission rate in the waveguide γ_0 is instead derived from the local density of optical states (LDOS) $\rho_0(r_0, \omega)$, for the TE0 waveguide mode:

$$\gamma_0 = \frac{\pi\omega|\mathbf{d}|^2}{3\hbar\varepsilon_0}\rho_0(r_0, \omega), \tag{S4}$$

where the LDOS is obtained from the dyadic Green's function $\overleftrightarrow{\mathbf{G}}(r, r', \omega)$ as follows:

$$\rho_0 = \frac{6\omega}{\pi c^2}\left[\mathbf{p}^{\mathsf{T}}\mathrm{Im}\overleftrightarrow{\mathbf{G}}(r_0, r_0, \omega)\mathbf{p}\right] \tag{S5}$$

In a waveguide without mirrors, the Green's function is [1, 2]:

$$\overleftrightarrow{\mathbf{G}}(r, r', \omega) = \frac{c^2}{\omega v_g N}\bar{\mathbf{E}}(y, z)\left[\bar{\mathbf{E}}^{\mathsf{T}}(y', z')\right]^* kG_0(x, x', \omega) \tag{S6}$$

with normalization factor $N = \int \varepsilon_r(y,z)|\bar{\mathbf{E}}(y,z)|^2 dydz$ and

$$G_0(x,x',\omega) = \frac{i}{2k} e^{ik|x-x'|} \tag{S7}$$

being the 1D scalar Green's function.

The mirror produces an image dipole at a position r'' located at a distance $2L$ from the dipole position along the x-axis, which results in a total Green's function:

$$\overleftrightarrow{\mathbf{G}}_{\mathrm{TOT}}(r,r',\omega) = \overleftrightarrow{\mathbf{G}}(r,r',\omega) \pm |r_{\mathrm{T}}| e^{i2\phi} \overleftrightarrow{\mathbf{G}}(r,r'',\omega), \tag{S8}$$

where the + holds for $x-$polarized dipoles and - holds for $y-$polarized dipoles due to the opposite reflection properties. The lifetime for a given dipole orientation is thus given by

$$\begin{aligned}\frac{\gamma_{x/y,\phi}}{\gamma_{x/y,0}} = \frac{\rho_{x/y,\phi}}{\rho_{x/y,0}} &= 1 \pm |r_{\mathrm{T}}| \frac{\mathrm{Im}\left[e^{i2\phi} G_0(0,2L,\omega)\right]}{\mathrm{Im}[G_0(0,0,\omega)]} \\ &= 1 \pm |r_{\mathrm{T}}| \cos(2\phi + 2kL).\end{aligned} \tag{S9}$$

which results in the expression provided in the main text Eq.1. We note that the change in lifetime is thus a direct manifestation of the change in LDOS. Importantly, this effect is very broadband, as ω does not play a significant role in the change of LDOS, in striking contrast with cavity-based approaches, where spectral tuning is essential to observe a change in the spontaneous emission rate. The equations above are derived under the assumption of single dipole excitation. In the experimentally relevant case of above-band excitation, both dipolar transitions are equally populated. The corresponding visibility is reduced to

$$v_\gamma = \left| \beta_{x0} \frac{\Gamma_{x0}}{\Gamma_{x0} + \Gamma_{y0}} - \beta_{y0} \frac{\Gamma_{y0}}{\Gamma_{x0} + \Gamma_{y0}} \right| |r_{\mathrm{T}}|. \tag{S10}$$

The decay rates of the x- and y-dipoles differ only slightly with the lateral emitter position, such that $\gamma_{x0} \simeq \gamma_{y0}$. For QDs located at the center of the waveguide, where $\beta_{x0} \simeq 0$, the visibility can therefore be approximated as $v_\gamma \simeq \frac{1}{2}\beta_{y0}|r_{\mathrm{T}}|$. The collected intensity is likewise modified by the combined contributions of the two dipoles (see Supplementary Information), yielding

$$v_{\mathrm{I}} = \frac{2|r_{\mathrm{T}}|}{1+|r_{\mathrm{T}}|^2} \left| \frac{|e_y(y_0)|^2 - |e_x(y_0)|^2}{|e_y(y_0)|^2 + |e_x(y_0)|^2} \right|. \tag{S11}$$

where e_x and e_y denote the normalized electric-field amplitudes of the waveguide eigenmodes at the emitter position y_0. Even when both dipolar transitions are addressed, the modulation depth remains a valid probe of the emitter-WG coupling strength, as discussed further alongside the experimental results.

B Phase-Shifter Design

This section presents the results of numerical simulations performed to determine the optimal geometry of the device shown in Fig. S2. The device consists of two symmetric cantilevers separated by a slot of gap (g). The inner cantilever is anchored to a mesa, whereas the outer cantilever is connected to a comb-drive actuator that enables tuning of the slot gap. Confining the optical mode within the slot requires substantially narrower waveguides than those used in the coupled-waveguide configuration. The device geometry must therefore balance the increased optical loss caused by sidewall roughness against the enhanced phase-modulation efficiency provided by stronger slot-mode confinement.

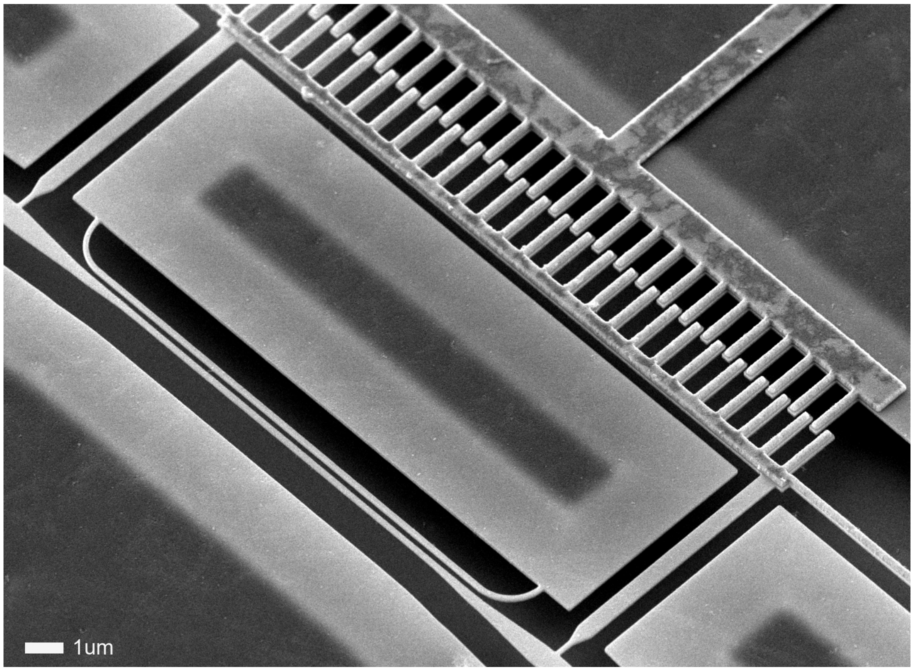

Figure S2: SEM image of the slot-mode waveguide phase shifter. The slot mode is formed by engineering the geometry of the two cantilever beams. Optical mode modulation is achieved by mechanically displacing one of the cantilevers through electrostatic actuation using the comb-drive actuator.

The accumulated phase shift, $\Delta\phi$, is simulated for the configuration shown in Fig. S2, with an active phase-modulation length of $L = 10$ µm. Both the cantilever width, w, and the slot initial gap are varied at a wavelength of 940 nm. A symmetric geometry is adopted, in which the inner and outer cantilevers have the same width. As expected, the phase shift responds asymmetrically when the cantilevers are pushed closer or pulled farther apart from their initial positions. Reducing the slot gap, corresponding to a negative displacement, produces a substantially larger phase shift than an equal positive displacement that increases the gap. Because fabricating devices with very narrow initial gaps is challenging, we operate in the pushing mode. This allows a larger initial gap to be used while still accessing strong phase modulation. Although narrower cantilevers are expected to enhance slot-mode confinement by increasing the fraction of the optical field within the slot, the simulations show that they do not necessarily maximize the phase response over the investigated range of slot gaps. Among the cantilever widths ranging from 130 to 170 nm, a width of $w = 150$ nm requires the smallest displacement to achieve a given phase shift at a given initial gap shown in Fig S3 a.

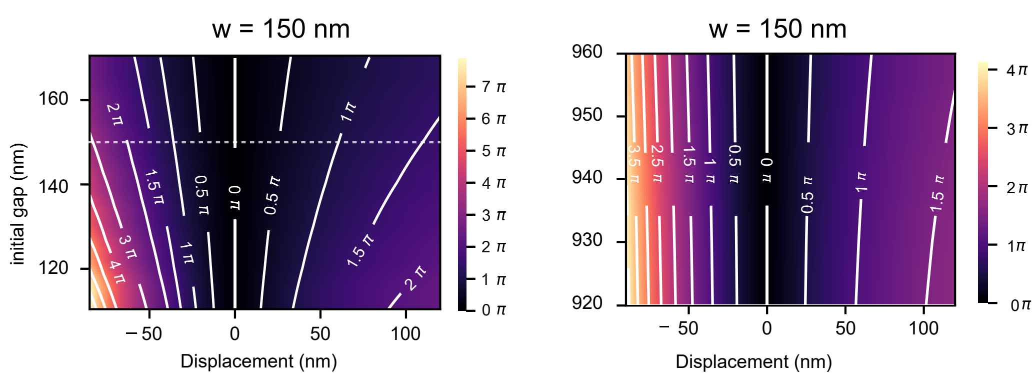

Figure S3: a. Absolute accumulated phase shift, $\Delta\phi$, as a function of the initial slot gap and cantilever displacement for a 10 µm-long GaAs slot waveguide with a cantilever width of $w = 150$ nm at a wavelength of $\lambda = 940$ nm. b. Phase response as a function of wavelength and cantilever displacement for an initial slot gap of 150 nm, corresponding to the white dashed line in a. The white contour lines in each panel indicate combinations of the initial slot gap and displacement in a, or wavelength and displacement in b, that yield the same accumulated phase shift.

The phase response is further simulated as a function of wavelength and the cantilever displacement for an initial slot gap of 150 nm seen in Fig. S3 b. To achieve a given phase shift, the required cantilever displacement initially decreases nonlinearly with increasing wavelength and then increases again at longer wavelengths. Thus, over the investigated parameter range, the displacement required to achieve a 3π phase shift is less sensitive to the initial slot gap than that required to achieve a π phase shift. To finalize the device design, we next simulate the actuation force required to produce a given positive or negative displacement of the slot waveguide.

C Electromechanical simulations

Actuation of the phase shifter is achieved through electromechanical displacement of the slot-waveguide cantilever. The actuator design is shown in Fig. S4a. To determine the displacement generated by the comb-drive actuator, we perform coupled electromechanical simulations. A deformable air domain is defined around the device to account for the electrostatic forces and the resulting mechanical deformation. An auxiliary sweep of the applied voltage is then performed to determine the voltage-dependent displacement.

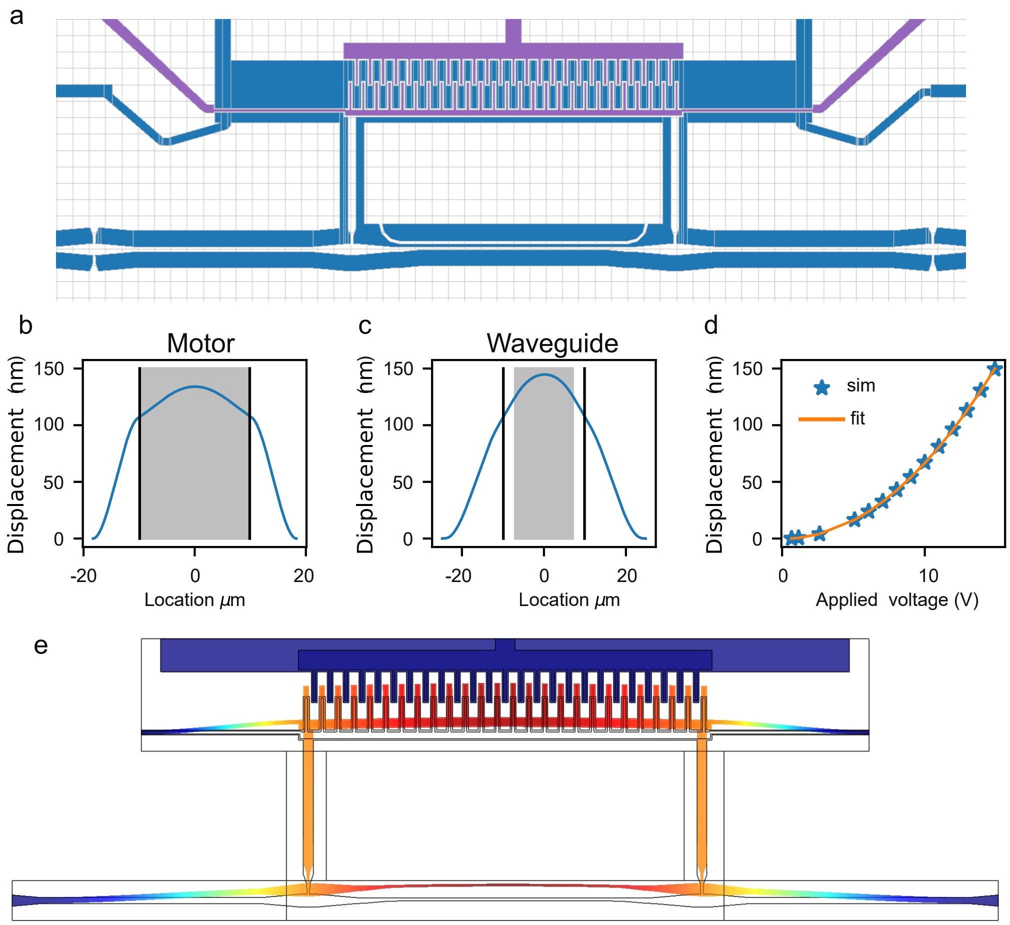

Figure S4: a. CAD layout of the comb-drive actuator designed to produce negative displacement of the slot waveguide. The device comprises a 10 µm-long cantilevers and 3.2 µm-long couplers. White, purple, and dark blue indicate the GaAs substrate, metal electrodes, and deeply etched regions, respectively. b. Displacement of the comb-drive actuator at an applied voltage of 15 V, with the center of the actuator along the light-propagation direction chosen as the coordinate origin. c.Corresponding displacement of the cantilever. d.Cantilever displacement as a function of applied voltage. e. Simulated displacement profile at 15 V, with the deformation visually exaggerated. To reduce the computational cost, the inner cantilever of the slot waveguide is omitted from the simulations.

The simulated electromechanical response of the comb-drive actuator is presented in Fig. S4(b-e). Fig. S4e. shows the spatial distribution of the displacement, which remains approximately uniform along the active section of the cantilever. Fig. S4b. shows the displacement of the comb-drive actuator. The black lines mark the positions of the tethers connecting the actuator to the slot-waveguide cantilever, while the shaded region indicates the position of the comb drive. The corresponding displacement of the slot-waveguide cantilever is shown in Fig. S4c. Here, the black lines mark the tether positions, and the shaded region indicates the slot-waveguide cantilever and the coupler. Fig. S4d. shows the cantilever displacement as a function of the applied voltage. The simulated response is fitted using

$$\Delta x = bV^2. \tag{S12}$$

where the fitted actuation coefficient is $b = 0.65\ \mathrm{nm\,V^{-2}}$. The quadratic voltage dependence is characteristic of electrostatic actuation. Because the present design uses a comb-drive actuator, the accessible displacement is not limited by the conventional pull-in instability of a parallel-plate actuator. Instead, it is ultimately limited by the initial gap between the two cantilevers. If the cantilevers are brought into contact, adhesion caused by van der Waals forces may lead to irreversible stiction, preventing them from separating when the voltage is removed. For an initial slot gap of $g_0 = 150$ nm, the voltage at which the displacement becomes equal to the initial gap is estimated as

$$V_{\mathrm{contact}} = \sqrt{\frac{g_0}{b_{\mathrm{comb}}}} = \sqrt{\frac{150\ \mathrm{nm}}{0.65\ \mathrm{nm\,V^{-2}}}} = 15.19\ \mathrm{V}. \tag{S13}$$

This value provides an upper estimate of the operating voltage at which the two cantilevers would come into contact. In the section above, the negative displacement required to produce a 3π phase shift at a wavelength of $\lambda = 940$ nm was found to be approximately 70–85 nm for a phase shifter with an active length of $L = 10$ µm and a cantilever width of $w = 150$ nm. To accommodate possible deviations arising from fabrication imperfections, we target a displacement range of 80–100 nm. The corresponding actuation voltages are

$$\begin{aligned} V_{80\ \mathrm{nm}} &= \sqrt{\frac{80\ \mathrm{nm}}{0.65\ \mathrm{nm\,V^{-2}}}} = 11.1\ \mathrm{V}, \\ V_{100\ \mathrm{nm}} &= \sqrt{\frac{100\ \mathrm{nm}}{0.65\ \mathrm{nm\,V^{-2}}}} = 12.4\ \mathrm{V}. \end{aligned} \tag{S14}$$

The target displacement range can therefore be reached at applied voltages of approximately 11.1–12.4 V, below the estimated contact voltage of 15.19 V.

D Optical setup and emitter characterization

The optical setup is illustrated in Fig. S5, where the excitation path is shown in light blue and the collection path in green. A 50/50 beamsplitter is shared by both paths, directing the excitation laser onto the sample and guiding the emitted photons toward the detector. A half-wave plate and a quarter-wave plate are introduced in the excitation and collection paths, respectively, to optimize light-coupling efficiency. To isolate the emission from a single QD, a grating filter is used.

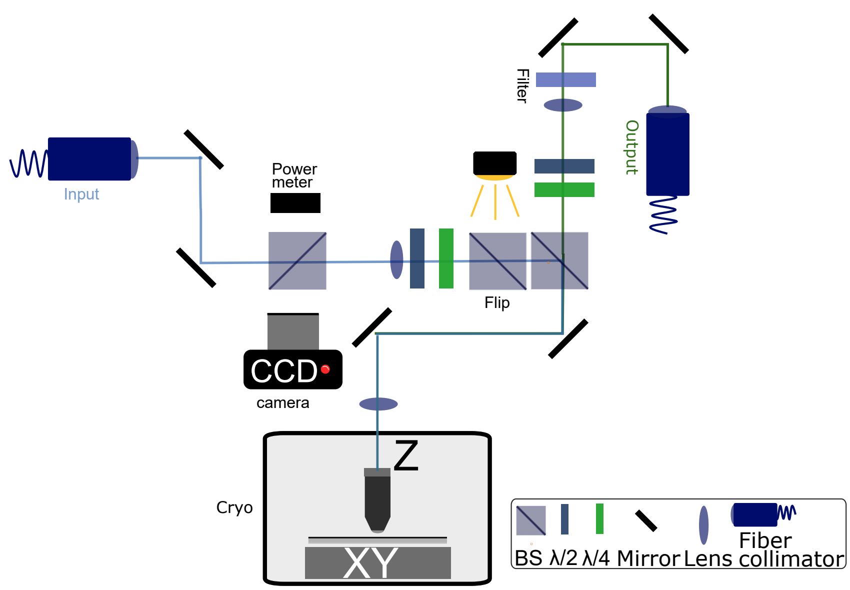

Figure S5: Schematic of the optical measurement setup. The legend identifies all optical components: BS denotes a 50/50 beamsplitter, $\frac{\lambda}{2}$ is a half-wave plate, and $\frac{\lambda}{4}$ is a quarter-wave plate. The lenses forming the 4f system have a focal length of 200 mm. The lens of the fiber collimator for both excitation and collection with a focus distance of 4 mm to achieve high collection efficiency.

Before performing time-resolved measurements on individual QDs, we characterize the saturation behaviour of each selected emitter. All subsequent measurements are conducted below saturation. Fig. S6 shows time-resolved intensity traces recorded at different applied voltages, using the same integration time for each measurement. A clear oscillation of the emission intensity with voltage is observed. As described in the main text, the voltage-dependent intensity is fitted with a sinusoidal function to extract the modulation contrast. For QD1, a higher intensity at early decay times coincides with faster spontaneous emission. The fitted decay rate therefore exhibits the same oscillatory behaviour as the intensity, as presented in Fig.4 of the main text. The lower panel shows a 2D view of the emission intensity as a function of decay time and squared applied voltage, V^2, further illustrating the modulation dynamics. Another emitter, denoted QD4 in the main text, is shown for comparison. After fabrication, QD4 is located close to a node of the standing optical field, whereas QD1 is located close to an antinode. QD4 exhibits a large intensity-modulation contrast of 0.79 and a moderate decay-rate modulation contrast of 0.17. The comparatively high maximum photon count rate further indicates that QD4 is located close to the centre of the waveguide and therefore couples efficiently to the guided mode. Its relatively small decay-rate modulation is attributed primarily to the small value of r_T, which varies with wavelength in the fabricated device owing to fabrication imperfections.

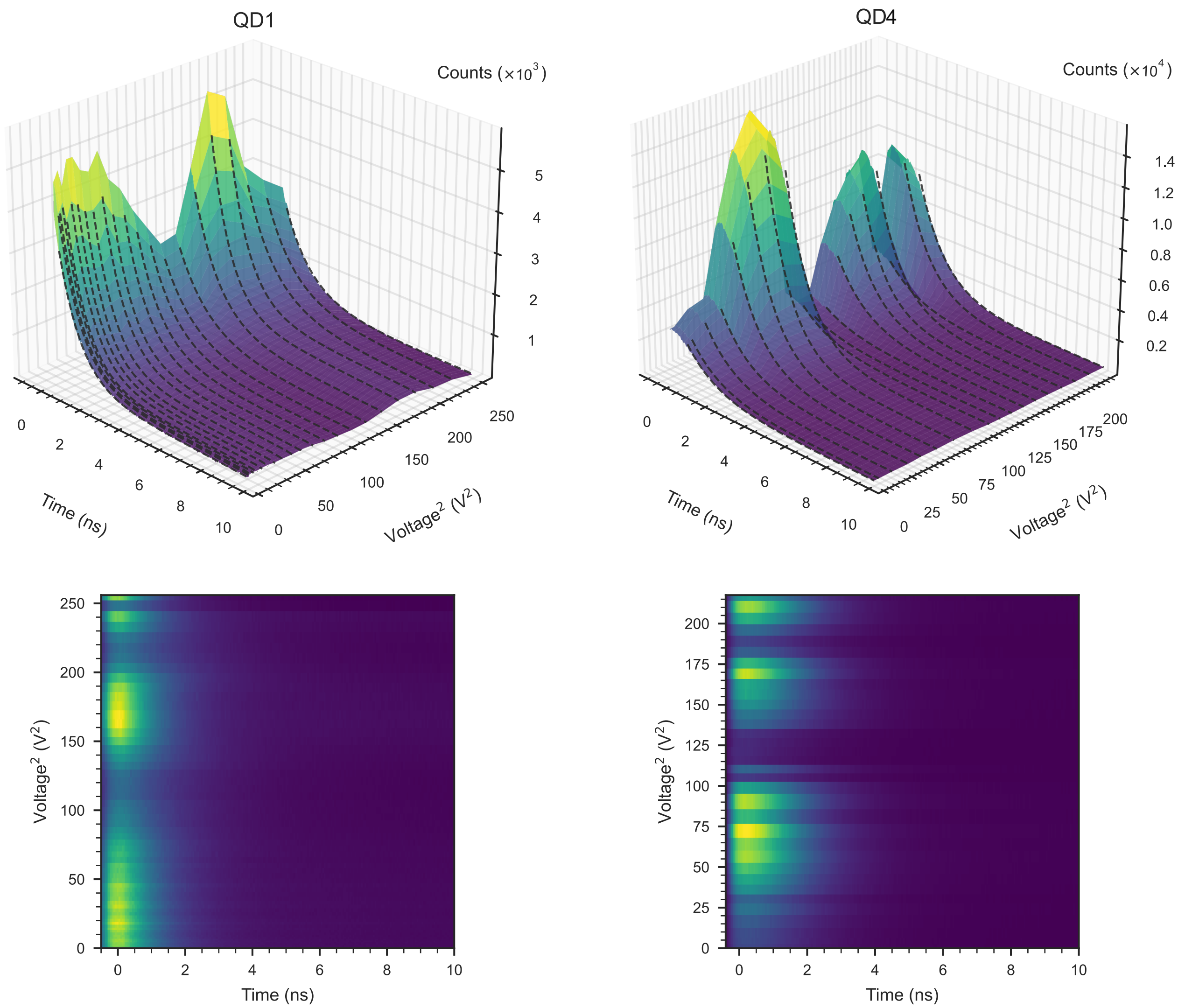

Figure S6: Time-resolved intensity as a function of the squared applied voltage, V^2, which is proportional to the phase shift ϕ, measured using the same integration time at each voltage. A clear modulation of the emission intensity is observed. The lower panels show the corresponding two-dimensional intensity maps as a guide to the eye. QD1 and QD4, as denoted in the main text, have emission wavelengths of 923.45 nm and 940.21 nm, respectively.

Supplementary References

[1] Jeppe Johansen, Brian Julsgaard, Søren Stobbe, Jørn M Hvam, and Peter Lodahl. Probing long-lived dark excitons in self-assembled quantum dots. *Physical Review B—Condensed Matter and Materials Physics*, 81(8):081304, 2010.

[2] Thomas Hümmer, FJ García-Vidal, Luis Martín-Moreno, and David Zueco. Weak and strong coupling regimes in plasmonic qed. *Physical Review B—Condensed Matter and Materials Physics*, 87(11):115419, 2013.